Journal of Catalysis 271 (2010) 59–66

Contents lists available at ScienceDirect

Journal of Catalysis

journal homepage: www.elsevier.com/locate/jcat

In situ synthesis and catalytic activity in CO oxidation of metal nanoparticles supported on porous nanocrystalline silicon

Sergej Polisski [a], Bernhard Goller [a], Karen Wilson [b], Dmitry Kovalev [a,*], Vladimir Zaikowskii [c], Alexei Lapkin [d,*]

[a] Department of Physics, University of Bath, Bath, UK
[b] Cardiff Catalysis Institute, School of Chemistry, Cardiff University, Cardiff, UK
[c] Boreskov Institute of Catalysis, Novosibirsk, Russia
[d] School of Engineering, University of Warwick, Coventry, UK

ARTICLE INFO

Article history:
Received 4 November 2009
Revised 14 January 2010
Accepted 1 February 2010
Available online 5 March 2010

Keywords:
Metal nanoparticles
Porous silicon
Nanocrystalline silicon
CO oxidation
Pt catalyst

ABSTRACT

Reactive surface of mesoporous nanocrystalline silicon was used to synthesise noble metal nanoparticles via *in situ* reduction of the precursor salt solutions. The synthetic methodology for metal nanoparticle formation was systematically developed, and reaction conditions of metal salts reduction were optimised to prepare nanoparticles of controlled size distribution in the order 5–10 nm inside the mesoporous silicon template. CO oxidation was used as a test reaction for the synthesised Pt/porous silicon catalysts. Sharp reaction light-off was observed at about 120 °C on the optimised catalysts. The catalysts were shown to be stable in the extended steady-state runs and in the catalysts re-use experiments. Metal nanoparticles were shown to be stable to sintering at elevated temperatures up to 1000 °C. However, after thermal treatment on air, Pt nanoparticles were covered by a SiO_x layer and were less active in CO oxidation.

1. Introduction

Metal catalysts play an important role in a wide range of chemical industries, from large-scale petrochemical processes, such as e.g. hydrotreatment and Fischer–Tropsch synthesis, to pollution abatement e.g. in three-way car exhaust catalysts, to fine chemical synthesis e.g. in selective hydrogenation and oxidation reactions [1,2]. In the majority of reactions, a support for highly dispersed active metals is an inert material, establishing a high surface area for active sites and possessing good mechanical, thermal and chemical stability. However, in a number of reactions, a support is an active component of a catalytic cycle [3]. The most widely appreciated examples are reducible oxides (CeO, TiO_2, etc.), which contribute to the electronic state of an active metal site during a catalytic reaction, supports promoting spillover of hydrogen, etc. [4]. Although effects of a support on catalytic reactions are normally secondary, i.e. through mass transport effects and the ability to disperse active component(s), and primary focus of catalytic science is aimed at discovery and design of active catalytic sites, there is an increasing appreciation of the potential for systematic design of electronic interactions between semiconductor supports and metal catalysts [5].

In this respect, porous silicon (PSi) is an interesting material, totally unexplored for catalytic applications. We have earlier reported initial findings on the catalytic activity of Pt/PSi [6]. Porous silicon is conventionally produced by electrochemical etching of doped electronic-grade wafers [7]. The resulting material is a sponge-like structure with an open-pore network with the mesopore-range of 2–6 nm [8]. Careful control of etching process allows one to 'design' the pore network to produce bi-modal or more complex spatial pore-size distributions within a material. The material's 'body' is constituted by nanocrystals, which retain crystal structure of the original single-crystal silicon wafer. It is the quantum-size effect, emerging from the crystal size dependent band-gap of semiconducting silicon nanocrystals, which is the most thoroughly investigated phenomenon, with potential applications in light emission, oxygen sensitising, etc. The potential interest of porous nanocrystalline silicon (PSi) as a support for metal catalysts stems from (i) the nature of chemical surface and porous structure of the freshly prepared PSi and (ii) from the semiconducting properties of Si.

(i) The extended surface area of PSi is hydrogen-terminated. This feature has been exploited for functionalization of porous silicon surface through sililation reactions [9], as well as to develop novel explosive materials [10]. Hydrophobic surface is also favourable for supporting enzymes [11,12]. The hydrogen termination of PSi surface can facilitate reduction of dissolved metal salts directly at the surface, without the

* Corresponding authors. Fax: +44 (0) 1225 386110 (D. Kovalev), +44 (0) 2476 418922 (A. Lapkin).
E-mail addresses: d.kovalev@bath.ac.uk (D. Kovalev), a.lapkin@warwick.ac.uk (A. Lapkin).

0021-9517/$ - see front matter © 2010 Elsevier Inc. All rights reserved.
doi:10.1016/j.jcat.2010.02.002

use of additional reducing agents, such as metal hydrides or molecular hydrogen [13–15]. This has been used earlier to produce metal nanoparticles from aqueous metal salt solutions. The resulting metal–silicon (M/PSi) composites contain relatively large metal nanoparticles on the external surface of porous silicon or represent a fully metallised external surface of silicon. Such materials are of little interest for catalysis, due to a too low metal dispersion and hence low specific catalytic activity. Metal nanoparticles on the surface of porous silicon were also prepared by sputtering [16]. In the present study, a method of synthesis of highly dispersed and uniform metal nanoparticles within the entire porous network of nanocrystalline PSi is developed.

(ii) Semiconducting catalyst supports have already been investigated extensively, due to the potential to directly influence the electronic state of a metal active site, see an overview in [3]. Recently, more experimental evidence of the importance of electronic interactions between supported metal nanoparticles and with the support was obtained using well-defined nanoparticle structures obtained by a laser electrodispersion method [17]. Thus, semiconducting properties of silicon and the ease of modification of its surface from conducting to nonconducting by oxidising to controlled thickness SiO_x layers is potentially very interesting from the point of view of model well-defined catalytic systems.

Porous silicon produced by chemical etching of wafers is far too expensive to be seriously considered as a viable support for catalysts. However, recent development of a process to produce porous silicon as a powder from widely available and relatively cheap metallurgical-grade Si [18] changes this situation radically.

In this study, we report the first systematic study of a method of preparation of active metal catalysts supported on porous silicon produced from low-cost metallurgical-grade silicon material. The paper is concerned primarily with synthesis of metal nanoparticles. A test reaction of CO oxidation was used to establish the uniformity of active sites and for comparison with other known metal-supported catalysts.

2. Experimental

2.1. Porous silicon preparation and characterisation

PSi layers were prepared via electrochemical etching of bulk B-doped (1 0 0) Si substrates with a typical resistivity of 2–10 Ω cm resulting in mesoporous Si with pore sizes in the range of 3–10 nm. The electrochemical etching was performed in a Teflon cell with a Pt wire as a cathode. A 1:1 (v/v) mixture of hydrofluoric acid (49 wt% in water) and ethanol were used as an electrolyte, with an etching current density of 30–50 mA cm^{-2}. The anodization time and current were varied in order to obtain different layer thicknesses, ranging from 20 to 200 μm, and having different porosities (65–80%).

To prepare H-terminated nanocrystalline PSi powders, we used a standard metallurgical-grade polycrystalline Si powder with a mean particle size of 4 μm. It was porosified via a stain-etching procedure described elsewhere [19,20]. Etching was finished when the initially grey colour of Si powder turned to brown-yellow and an efficient red-orange emission, under ultraviolet illumination of a dried aliquot, appeared. Due to the quantum confinement effects, this emission clearly indicates the presence of nanocrystals with the crystal sizes below 10 nm [21].

Hydrogen desorption experiments on as-prepared PSi powders were carried out in a tubular oven at elevated temperatures. The level of hydrogen termination of PSi surface was evaluated using Fourier-transformed infrared (FTIR) spectroscopy (Bruker Equinox 55). To regain surface H-termination of PSi powder after hydrogen desorption, samples were immersed in a 5% (v/v) solution of HF in iso-propanol. The powder was then washed using iso-propanol and water and dried in hydrogen flow.

2.2. Preparation and characterisation of M/PSi and M/PSiO_x materials

After the etching procedure, PSi powder was evacuated for 2 h at 90 °C to evaporate etching residues such as HF from the pores. $PtCl_4$ salts in HCl (platinic acid H_2PtCl_6) dissolved in an alcohol were used as a precursor for metal NPs' formation. Alcohol solvents were used to attain wetting of the hydrophobic H-terminated surface of PSi. In these experiments, we utilised methanol, ethanol or iso-propanol, respectively, with salt concentrations between 0.1 and 20 mM, resulting in Pt loadings between 0.1 and 5 wt% with respect to the amount of PSi.

PSi samples were introduced to the Pt salt solutions at a fixed low temperature in the range between −20 and 0 °C. The suspensions were kept for 20 min in an ultrasonic bath and then left to reach ambient temperature under gentle mechanical stirring. HCl vapour evolution upon immersion of as-prepared PSi layers into an alcohol–Pt salt solution was detected. Completion of the metal reduction reaction was monitored by a wet universal pH indicator paper brought in contact with the evolved gas. Following the metal NPs' formation, reaction samples were heated to 40 °C, while stirred to ensure slow solvent evaporation. The obtained Pt/PSi materials were further dried at room temperature, washed several times with ethanol and warm water (50 °C) to dissolve possible remnant salts in the pores. pH of the residual alcohol solutions was monitored after each washing step until the supernatant solution was pH neutral. The prepared Pt/PSi samples were separated by centrifugation for 10 min at 5000 rpm.

The Pt/PSiO_x samples were prepared by annealing of the as-prepared Pt/PSi composites in a tubular oven at 1100 °C for a set period of time, 2, 3, 6 and 12 h on air.

The amount of deposited metal was determined by analysing the collected supernatant solutions by the Atomic Adsorption Spectroscopy (AAS, Varian AA-275) directly after M/PSi preparation.

To study the penetration depth of the precursor salt solutions into the PSi matrix, and hence, the location of the formed metal nanoparticles, 150- to 200-μm-thick PSi layers were used. These flat PSi layers have almost identical morphology to that of the PSi powders used in this study. We have chosen Au salt precursors for this, since the colour appearance of metallic Au NPs can be easily distinguished from the colour of PSiO_x layers: plasmon resonance of Au NPs is in red spectral range. PSi layers were dropwise wetted by an alcoholic $HAuCl_4$ solution (60 mM) having a 2 wt% Au ratio with respect to the PSi support. Au deposition was performed at fixed temperatures within the range between −5 and 65 °C. Penetration depth of Au was measured on a cleaved edge of the Au loaded oxidised PSi layers using an optical microscope.

2.3. Catalysts characterisation

Transmission electron microscopy (HRTEM) images were obtained using a JEM-2010, JEOL instrument. X-ray photoelectric spectroscopy (XPS) measurements were performed on a Kratos Axis HSi instrument employing a Mg Kα X-ray source and charge neutraliser. Survey scans and high resolution scans were acquired at normal emission using analyser pass energies of 160 and 40 eV, respectively. Pt 4f spectra were deconvoluted with components having an asymmetrical "Doniach–Sunjic" [22] line shape. Nitrogen adsorption–desorption isotherms were measured at 77 K using

Micromeritics 2010 instrument. The BET surface area was calculated from adsorption isotherms between 0.08 and 0.4 $P\ P_0^{-1}$ (where P is the equilibrium gas pressure, P_0 is the saturation vapour pressure). The pore-size distribution was calculated by Barrett, Joyner and Halenda (BJH) method from desorption isotherm between 0.8 and 0.9 $P\ P_0^{-1}$ as described in [23].

A Micromeritics PulseChemisorb 2700 surface area analyser was used to determine metal dispersions (fraction of surface Pt atoms) using H_2 chemisorption. Samples were reduced at 400 °C under flowing H_2 for 1 h prior to dispersion measurements. The amount of deposited Pt in PSi and $PSiO_x$ supports was calculated on the basis of AAS data and metal dispersion data, obtained from H_2 chemisorption experiments.

2.4. Catalytic experiments

Pt/PSi composites based on PSi powders were pre-treated in hydrogen flow at 5 $cm^3\ min^{-1}$ at 290 °C (P = 1 bar) for 2 h immediately prior to catalytic experiments. Since the as-prepared samples already contain metallic or partially oxidised Pt nanoparticles reduced by surface protons of fresh PSi powders, the pre-treatment was done without special care to avoid mobility of Pt precursors, as in the case of the catalysts obtained by reduction of hexaplatinic acid [24,25]. Similar pre-reduction procedures were used by other groups [26]. All catalysts were treated in the same way.

CO oxidation experiments were performed in the temperature range 25–300 °C using 1% CO/20% O_2 (v/v) balanced by helium reaction mixture. In all experiments, gas flow rate was 75 cm^3 (STP) min^{-1}. Catalysts 0.3 g Pt/PSi mixed with 0.15 g crushed quartz were supported on a glass wool bed in a quartz U-tube reactor. A gas-sampling mass spectrometer (Micromass, European Spectrometry Systems) was utilised to trace the CO_2 output of the monitored reactions. The turnover frequency (TOF) was calculated at 10% CO conversion, and also at a specified temperature and variable conversions. Details are given in the text.

Turnover frequency (TOF) was determined from the following formula:

$$\mathrm{TOF}_{exp} = \frac{\mathrm{C}[\mathrm{CO}_2, 10\%] \times F \times N_A}{N_{\mathrm{Pt}} \times D_{\mathrm{Pt}}} \quad (1)$$

where $C[CO_2]$ is the concentration of produced CO_2 at specified conversion (mol cm^{-3}), F is the total gas flow rate (cm^3 (STP) min^{-1}), N_A is the Avogadro's number, N_{Pt} is the total number of Pt atoms in a Pt/PSi catalyst derived from AAS measurements and D_{Pt} is the dispersion of Pt measured using H_2 chemisorption from a Pt/PSi catalyst.

3. Results and discussion

3.1. Morphology of PSi supports

The stain etching of p-doped metallurgical quality polycrystalline Si powder results in an open sponge-like structure consisting of nanometre-sized Si crystals and nm-range pores, see an HRTEM image in Fig. 1A. A higher resolution image shows that following etching the produced nanosized crystallites retain diamond-like lattice of bulk Si, see Fig. 1B. From the image, the size of continuous lattice fragments, corresponding to crystallites, could be estimated to be less than 5–8 nm. Thus, porosity is originating due to spaces between crystallites. The mean pore size can be varied via preparation conditions, such as the temperature, time and chemistry of the etching solution.

Fig. 2A shows the nitrogen isotherm measured for an as-prepared PSi powder, as-prepared Pt/PSi catalyst and as-prepared Pt/$PSiO_x$ catalyst, measured at −196 °C. The isotherms show a hysteresis in the area of 0.65–0.85 $P\ P_0^{-1}$ characteristic for mesoporous materials. The hysteresis of the parent material PSi is relatively narrow along the x-axis, which indicates that the pore network is open and pores are easily accessible. For comparison, in case of the ordered mesoporous silica, like SBA-15, having nearly straight, open pores, a similar hysteresis was observed, whereas for an amorphous porous silica obtained by a sol–gel synthesis route, the desorption curve is considerably more shallow [27]. The estimated BET surface area of the stain etched PSi powder is ~160 $m^2\ g^{-1}$, similar to values measured for PSi prepared from bulk Si wafers [28], with the pore volume of mesopores *ca.* 0.3 $cm^3\ g^{-1}$.

The pore-size distribution of the PSi powder is shown in Fig. 2B. The mean pore diameter is estimated to be ~7 nm, which is similar to the pore sizes of some other mesoporous catalyst supports, such as SBA-15 or some mesoporous carbons [27], whereas the pore-size distribution of PSi powders appears to be broader.

Deposition of Pt nanoparticles inside the porous silicon support results in a dramatic reduction of the specific surface area determined by nitrogen sorption: from 160 to 92 $m^2\ g^{-1}$ and the pore volume reduces from 0.3 to 0.23 $cm^3\ g^{-1}$. This is clearly seen also by the lower position of isotherms, see Fig. 2A. The mean pore size is also slightly reduced to ca. 6 nm. This suggests that metal is deposited inside the mesopores, reducing specific surface area and the amount of larger pores is reduced, shifting distribution

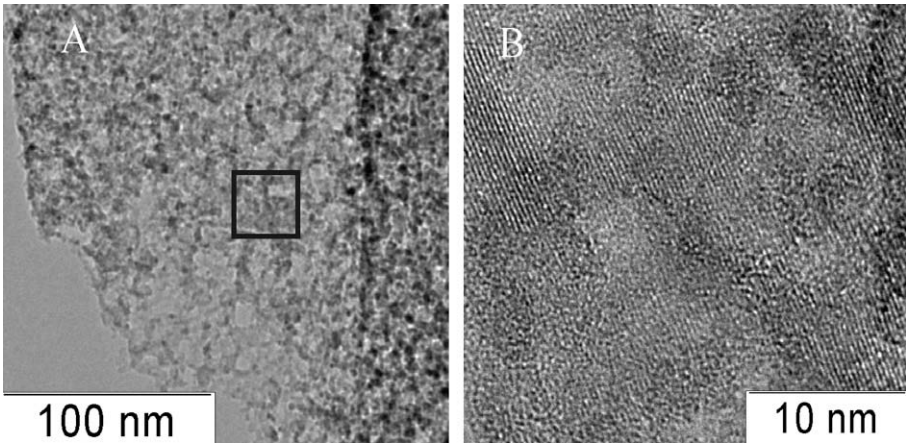

Fig. 1. TEM images of stain etched Si powder. (A) A low resolution image. (B) Magnified image of the material, marked by a square in (A).

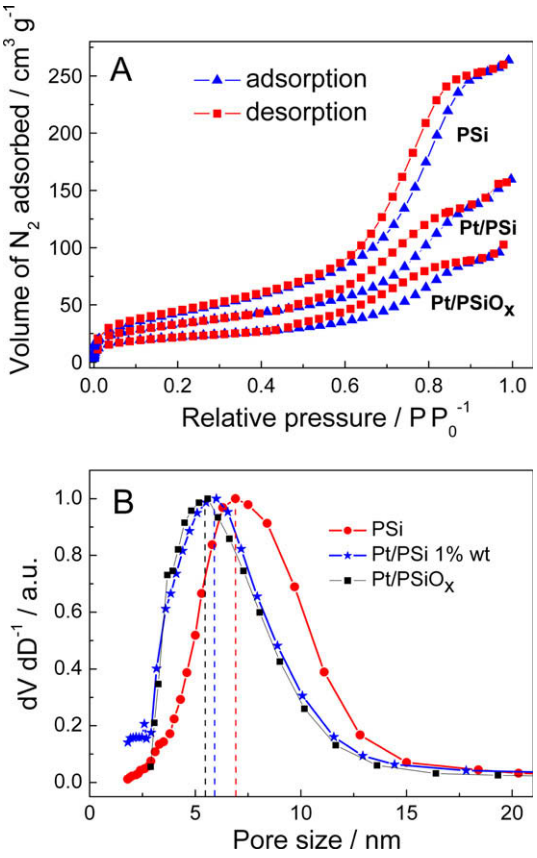

Fig. 2. Low temperature nitrogen sorption on 'as-prepared' porous silicon, fresh Pt/PSi and fresh oxidised Pt/PSiO_x catalysts. (A) Adsorption–desorption isotherms. (B) Pore-size distribution calculated using BJH method.

of pore sizes to more narrow pores. Thus, the size of metal nanoparticles should be in the order of 6–8 nm.

Following the high-temperature oxidation process of Pt/PSi catalyst, there is only a small structural change detected by nitrogen sorption data. Specific surface area calculated using a BET model is reduced from 92 $m^2\ g^{-1}$ for the Pt/PSi sample to 70 $m^2\ g^{-1}$ following the oxidation, and the pore volume of mesopores reduced from 0.23 to 0.15 $cm^3\ g^{-1}$, although the mean pore diameter effectively does not change: there is only a minor further shift of pore-size distribution to the more narrow pores, see Fig. 2B. This suggests a reduction in the number of pores, rather than a change in morphology. The HRTEM data presented in the following paragraph show the growth of SiO_x over-layers in the oxidised sample on top of Pt nanoparticles, which suggests that these structures lead to pore blockage and the corresponding reduction in the number of pores, detected by nitrogen sorption.

The surface termination of PSi supports has a significant influence on their reductive potential. Instability of hydrogen termination of PSi under heat treatment or strong oxidising conditions was reported earlier [29]. Fig. 3 shows a FTIR spectrum of a typical PSi sample exposed to air. The dominating surface groups identified from the spectra are Si–H, Si–H_2 and Si–H_3 bonds. Fig. 3A shows Si–H bending (625 cm^{-1}) and Si–H_2 wagging (662 cm^{-1}) vibration modes for these different types of PSi samples. In Fig. 3B, the stretching modes of Si–H_x bonds (2084 cm^{-1}, 2015 cm^{-1} and 2145 cm^{-1} for $x = 1$, 2 and 3, respectively) are also indicated [30]. A feature related to the Si–O–Si asymmetric stretching mode (1072 cm^{-1}), caused by surface oxidation of PSi powder on air, can also be clearly seen in the spectra. Its magnitude is larger than the Si–H_x-related absorption features due to the much higher oscillator strength of Si–O bonds.

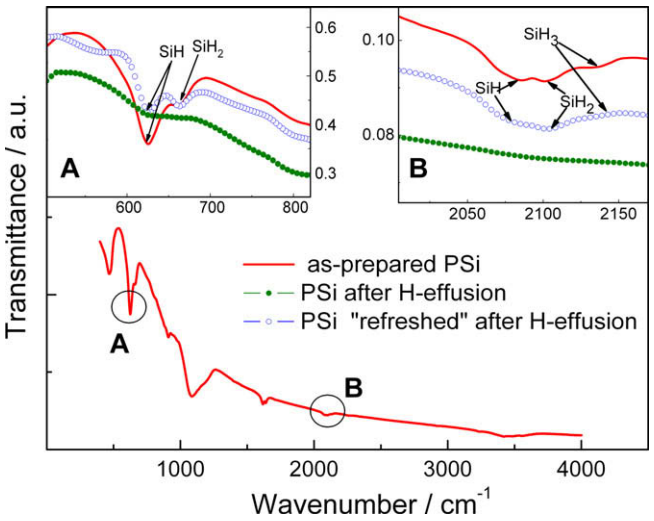

Fig. 3. FTIR transmission spectrum of an as-prepared PSi powder.

The insets A and B in Fig. 3 show evidence of the surface Si–H_x groups in three different samples: (i) the as-prepared PSi powder, (ii) the PSi powder after hydrogen effusion and (iii) the PSi sample immersed in the HF-containing solution following hydrogen effusion (identified as "refreshed" in Fig. 3). The second sample lacks Si–H_x groups; the absence of the corresponding bands is evident in the insets A and B in Fig. 3. However, an annealed sample partially regains hydrogen passivation after immersion in the HF-containing solution.

To emphasise the importance of hydrogen termination of the PSi support for metal salt reduction, a comparison of H-terminated PSi templates and those lacking H-termination after thermal hydrogen effusion was performed. While for the H-terminated samples, efficient metal nanoparticles formation was observed, no reductive activity was detected for the second type of samples. This evidences that the surface Si–H_x groups act as reductive agents in the metal nanoparticles formation in a hydrogen passivated PSi matrix.

3.2. Distribution of Pt within PSi support

Formation of metal NPs on PSi surfaces from aqueous metal salt solutions by *in situ* reduction was reported earlier [23,24]. However, since H-terminated PSi surface is strongly hydrophobic [31], aqueous metal salts cannot penetrate into the pores of PSi and nanoparticles are formed exclusively on the outer surface of a silicon support. This negates one of the advantages of the material, its extended surface and accessible pores in the mesopore range. Furthermore, metal nanoparticles formed on the outer surface of porous silicon (PSi) tend to be large due to the lack of the pore-constraint effect.

In order to obtain highly active catalytic systems, we have chosen alcoholic solutions of metal precursors to assure wetting of pores surface within the H-terminated PSi matrix. This should ensure formation of NPs uniformly throughout the PSi matrix. To determine the depth of metal NPs' formation, metal reduction was performed using the electrochemically etched thick PSi layers, fabricated from 1 0 0 orientation wafers. The wetting and reducing characteristics of the electrochemically etched PSi layers and of the stain etched powders are almost identical due to the similar pore morphology and surface termination. Penetration depth experiments were performed with aqueous and ethanol metal salt solutions, and using optical microscopy for visualisation.

Reaction temperature was found to be the key parameter determining the size and homogeneity of distribution within PSi matrix of the formed nanoparticles. Fig. 4A shows that at high temperatures, micrometre-sized metal islands, which are shown as bright spots in the image, are formed mainly on the surface of PSi layers. Similarly, at high salt concentration, the salt solutions also appear to be reduced before penetrating into the PSi matrix, which results in the formation of large Au surface islands (images are not shown). Complete surface metallisation can be achieved at sufficiently high salt concentrations or temperatures. At a lower temperature, 45 °C in Fig. 4B, gold islands are still present on the surface, however, with a lower density. Only at the lowest temperatures examined (−5 °C), no visible macroscopic surface Au aggregates could be detected, see Fig. 4C. At this temperature, due to a very slow reduction rate, the PSi matrix is filled homogeneously with the salt solution which is then reduced uniformly. This is clearly seen in the cleaved edge image in Fig. 4D. Under these conditions, the maximum depth at which gold nanoparticles were observed within the PSi layer was 120 μm. In a similar experiment at a low deposition temperature but using an aqueous precursor salt solution, the maximum depth within the support layer at which nanoparticles were found was 3 μm.

3.3. Morphology of Pt clusters on PSi and $PSiO_x$ supports

Examples of HRTEM images of a Pt/PSi catalyst synthesised at −5 °C are shown in Fig. 5. Several nanoparticles of a very similar size can be observed in Fig. 5A and B, illustrating the homogeneity of the formed Pt NPs. These are representative images from a large collection showing statistical significance of the determined particle sizes. The mean size of the nanoparticles determined from the images was found to be *ca.* 5–8 nm, see Fig. 5B. This corresponds well with the suggested size-range of metal nanoparticles on the basis of nitrogen sorption. Furthermore, in Fig. 5C, a well-defined crystalline structure of a Pt NP is shown. The measured lattice constant corresponds to crystalline Pt. In Fig. 5D, an X-ray diffraction pattern of a single Pt particle shows its crystalline nature with several well-defined crystal directions: [1 1 1], [2 0 0], etc.

High-temperature oxidation of Pt/PSi was performed in order to study thermal stability of the catalysts. During oxidation on air at

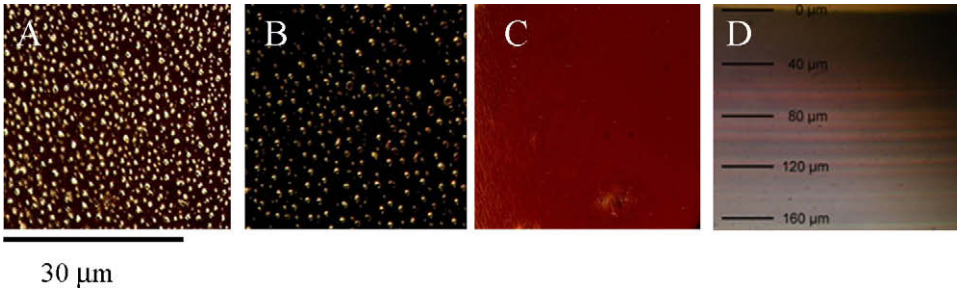

Fig. 4. Images of PSi layers containing Au NPs formed at different temperatures: (A) 65 °C, (B) 45 °C and (C) −5 °C, respectively, using $HAuCl_4$ (60 mM, 2 wt%) dissolved in ethanol; (D) cleaved edge image of the sample shown in (C).

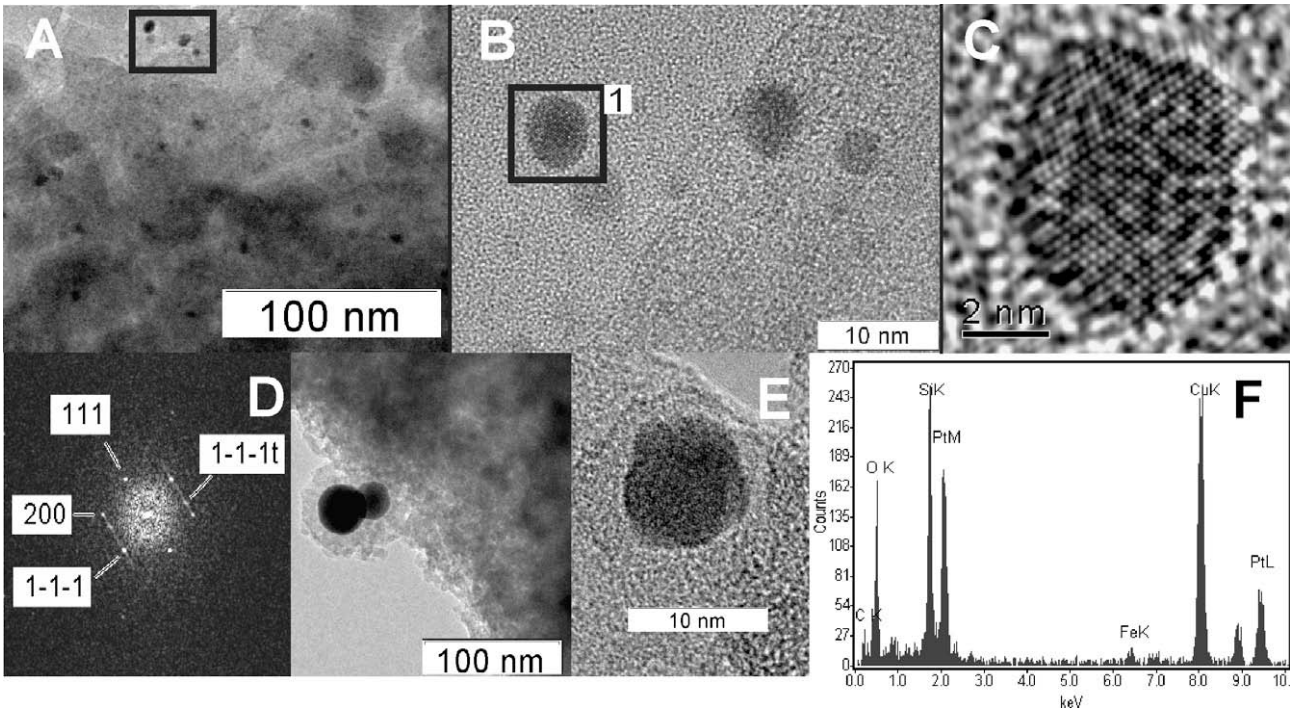

Fig. 5. HRTEM images of the 0.9 wt% Pt/PSi catalyst. (A) Low resolution image. (B) The magnified area shown in (A). (C) Magnified image of a Pt NP, imbedded in PSi matrix, marked by 1 in (B). (D) X-ray diffraction pattern of the same NP as the image in (C). (E) TEM of Pt NPs in a $PSiO_x$ matrix, formed via oxidation of 0.9 wt% Pt/PSi in air at 1100 °C for 6 h; two images of a Pt NP on the outer surface of a PSi particle and inside the pore structure. (F) EDX spectra of sample (E).

1100 °C, porous silicon support is almost completely converted to the oxide $PSiO_x$. An image of a single Pt particle located at the surface of oxidised PSi crystallite (at 100 nm resolution) and an image of a particle inside the oxidised PSi matrix are shown in Fig. 5E. A Pt nanoparticle located on the surface of a silicon particle is seen with a much better contrast between silicon, an oxide and Pt. This particle is significantly larger than the nanoparticles inside the PSi matrix. The majority of Pt particles are within the silicon structure, where an oxide layer can also be seen in the TEM image 5E, but with a less clear contrast.

The size of metal NPs inside the matrix is almost unaffected in comparison with the mean Pt nanoparticle size of the original catalysts, shown in Fig. 5B, and in contrast to the Pt particle shown on the surface of $PSiO_x$ matrix. This suggests that inside the pores, there is very little metal sintering even at such high temperatures and extended exposure. However, there is clear evidence of an oxide over-layer covering metal nanoparticles. The visibly different structure of amorphous material around Pt nanoparticles may correspond to SiO_x, Pt oxide or potentially a Pt silicide layer. The EDAX image shown in Fig. 5F shows signals of oxygen, silicon, platinum and iron. The presence of iron is attributed to the impurities in the metallurgical-grade silicon. Resolution of the EDAX instrument (130 eV) does not allow to directly identify the layer covering Pt nanoparticle as SiO_x or PtO_x.

3.4. XPS characterisation of as-prepared Pt/PSi catalysts

Fig. 6 shows Pt 4f XP spectra of the series of Pt/PSi samples, which reveal that at low Pt loadings two peaks are observed at 73 and 76.3 eV, which are attributed to the spin–orbit split Pt $4f_{7/2}$ and $4f_{5/2}$ states, respectively. Pt 4f spectra were deconvoluted with components having an asymmetrical Doniach–Sunjic line shape, represented by dotted lines. Concentration of these states increase steadily with metal loading up to ~1 wt% Pt. Higher Pt loadings result in the appearance of a new set of doublets at a lower binding energy with $4f_{7/2}$ and $4f_{5/2}$ components at 71.7 and 75 eV. The decrease in binding energy from PtO and PtO_2 to metallic Pt is expected to be ~1.3 and 2.7 eV, respectively [32]. In contrast, binding energy associated with PtSi or Pt_2Si bonds should show the increases of ~1.4 and 0.9 eV relative to metallic Pt [33]. The observed shift of 1.3 eV is believed to correspond to the transition from PtO to Pt^0. Given that the Pt/PSi catalysts were not heated above 100 °C during preparation, formation of silicide is unlikely.

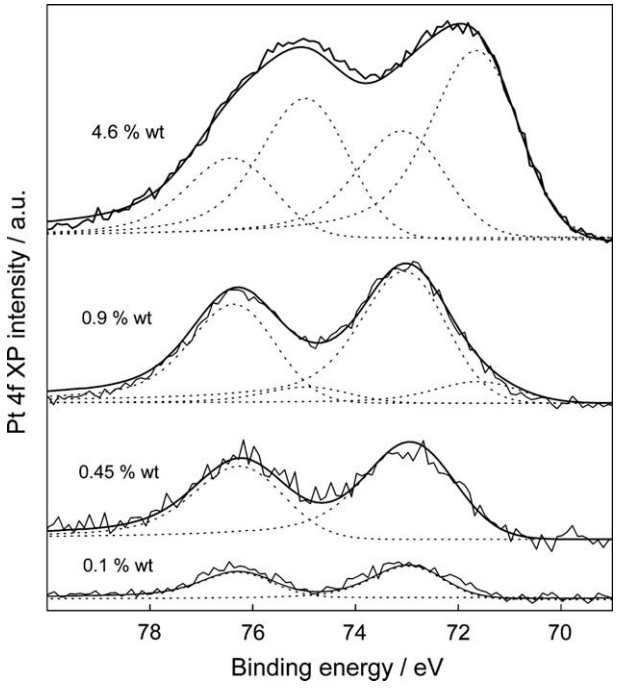

Fig. 6. Pt 4f XP spectra of as-prepared Pt/PSi catalysts with initially anticipated metal loadings. Dotted lines correspond to asymmetrical Doniach–Sunjic lineshape deconvolution for 4f Pt and PtO states.

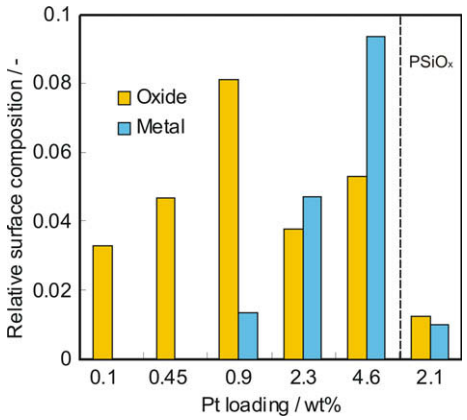

Fig. 7. Variation of surface Pt composition of as-prepared Pt/PSi and $Pt/PSiO_x$ catalysts having different metal loadings. Data were determined from deconvolution and quantification of XPS Pt 4f spectra. Pt loading was adjusted according to AAS measurements.

The distribution of oxide and metal states as a function of Pt loading for Pt/PSi samples, as well as for the oxidised 2.1 wt% $Pt/PSiO_x$ sample, is shown in Fig. 7. Following high-temperature oxidation, a significant decrease in Pt-related signal is observed. Simultaneously, an increase in the relative intensity of the oxide-related feature is observed. Attenuation of the Pt-related signal can be attributed to the formation of silicon dioxide and platinum oxide capping layer following high-temperature oxidation as evidenced by HRTEM (see Fig. 5E). This cannot be attributed to the growth of metal nanoparticles, since this would not explain the increase in oxygen signal. We cannot completely exclude formation of platinum silicide.

3.5. Catalytic activity of Pt/PSi and $Pt/PSiO_x$ in CO oxidation

CO oxidation reaction was used to test activity of the prepared Pt/PSi and $Pt/PSiO_x$ catalysts. Results are shown in Fig. 8. The 'as-prepared' PSi support without metal was used as a negative control to show no CO conversion (black curve, Fig. 8). A negligible conversion of CO was registered above 300 °C, which most probably results from hydrogen desorption taking place at these temperatures [33]. Due to the presence of unsaturated bonds in the peripheral PSi sites formed after hydrogen effusion, a small amount of CO and O_2 molecules can be adsorbed at these sites and further react to form carbon dioxide.

A sharp step in CO conversion was observed for all catalysts tested with Pt loading above 1 wt%. The light-off temperature (T_L) was between 110 and 130 °C. Here, 'light-off' denotes the temperature point of the maximum change in the reaction rate, corresponding to infinity in the derivative of conversion with respect to temperature. It is obtained graphically by locating the steepest gradient of the curves and extending it to intercept with the *x*-axis. This observation is in agreement with XPS data: metallic Pt is present in the catalysts only at metal loading above 1 wt%. The sharpness of the light-off curves for these catalysts is indicative of good uniformity of metal active sites. This is most likely associated with the narrow distribution of Pt NPs' sizes achieved through con-

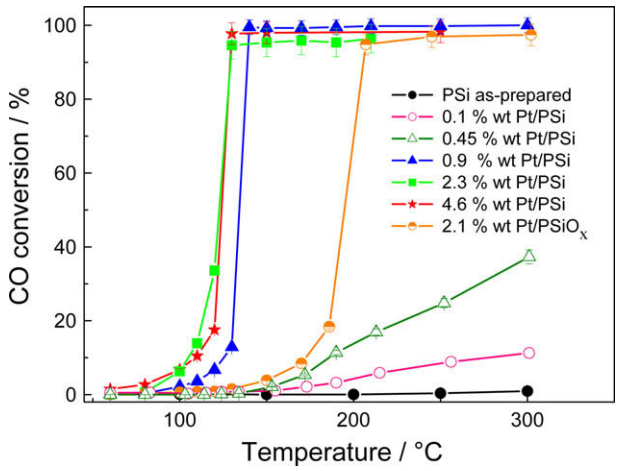

Fig. 8. CO conversion as a function of temperature for different Pt/PSi and Pt/PSiO_x catalysts.

trolled synthesis at low temperatures and assisted by the pore restriction.

For the catalysts with low Pt loadings, only low catalytic activity is observed, which is consistent with metal being primarily in the oxide state. This correlates with the literature data: platinum oxides have been reported to be only partially active in CO oxidation, with a much lower activity in comparison with metallic Pt [34]. Table 1 summarises values of metal dispersion, TOF and T_L for different samples. TOF was calculated for different temperatures and the same conversion (10%) and for different, but always low, conversions at the same temperature. The latter series of data allow more reliable comparison within the series of catalysts.

The observed data compare favourably with some literature Pt nanoparticle catalysts tested under similar conditions. TOF values in the range of 108–36 h^{-1} were reported for 0.96 wt% Pt/SiO_2 catalysts at 177 °C, values decreasing upon catalyst deactivation [26], which is lower than Pt/PSi 0.9 wt% catalyst, for which TOF of 193 was measured at 130 °C and 10% conversion. Similar or higher light-off temperatures were observed in the case of 1 wt% Pt/ZrO_2 catalysts, with the TOF values in the order of 360 h^{-1} at 127 °C in 1.5 times excess oxygen conditions [35]. This is better than the results for our 0.96 wt% catalyst and very close to the TOF values obtained with the 2.3 wt% Pt catalyst at a slightly lower temperature, see Table 1. The reported light-off curves for the well-defined Pt/ZrO_2 catalysts also exhibit very sharp increase [35], which was observed in this study for the Pt/PSi catalysts.

Pt nanoparticles synthesised *via* a conventional chemical reduction in solution and stabilised on SiO_2 particles or on glass surface, as well as reduced radiolitically were active only above 150 °C [36]. The reported volumetric rate of 0.13 mol l^{-1} h^{-1} (175 °C, O_2:CO = 16:1) corresponds to a TOF value of 510 h^{-1}. The TOF value is higher, but the catalyst was active only at a much higher temperature. In the case of Pt/Al_2O_3 catalysts in an excess of carbon monoxide (10% CO conversion, 207 °C, O_2/CO = 1:4), a TOF value of ~180 h^{-1} was reported [37].

Table 1
Catalytic activity of selected Pt/PSi and Pt/PSiO_x samples.

Sample (see Fig. 8)	Dispersion[a] /%	TOF[b] /h^{-1}	TOF[c] /h^{-1} (°C, %)	T_L /°C
0.1 wt% Pt/PSi	–	–	–	200
0.9 wt% Pt/PSi	6.2	193	63 (110, 4%)	130
2.3 wt% Pt/PSi	1.4	344	399 (110, 14%)	115
4.6 wt% Pt/PSi	2.6	41	41 (110, 10%)	110
2.1 wt% Pt/PSiO_x	1.54	363	482 (180, 15%)	180

[a] Measured by hydrogen chemisorption.
[b] TOF calculated at 10% CO conversion, see Eq. (1).
[c] TOF calculated at a given temperature and different conversions; temperature and conversion are specified in brackets.

The 2.3 wt% Pt/PSi catalyst system for which a complete CO conversion is reached at 120 °C with a TOF (at 14% conversion, 110 °C) of 399 h^{-1} is the most active catalyst synthesised in this study (see Table 1). The 0.9 wt% Pt/PSi catalyst attains complete CO conversion at slightly higher temperatures and shows a lower activity, with a TOF of 63 h^{-1} at 4% conversion, 110 °C (see Table 1), compared with the 2.3 wt% Pt/PSi catalyst. This is consistent with the XPS data, which show a considerably higher proportion of PtO surface species in the catalyst sample containing 0.9 wt% Pt.

Further increase in Pt loading to 4.6 wt% does not result in a higher catalytic activity despite the continuing trend to the increasing metallic character of surface Pt species, see Fig. 7. In fact, the TOF at the same temperature is much lower. This is due to the lower dispersion of Pt in the highly loaded samples.

The catalysts with Pt content below 0.9 wt% show a much lower catalytic activity, see Fig. 8. Notably, the light-off temperatures for the catalysts with 0.1 and 0.45 wt% Pt are similar to those for the oxidised catalysts with the higher metal loading. This suggests that active species in such catalysts could be similar, and the oxidised catalysts contain PtO_x species. The oxidised catalyst shows a reasonable activity with TOF at ca. 482 h^{-1}, but at a much higher temperature of reaction.

3.6. Catalysts stability

Stability of the Pt/PSi catalysts was tested in continuous runs over 20 h in the microreactor system at a maximum conversion. Repeated experiments were also performed with one of the catalysts. Results for the first and third runs with the same 0.9 wt% Pt/PSi catalyst are shown in Fig. 9, which show no decrease in the steady-state CO conversion over 20 h and no change in the level of conversion between the runs. This suggests that even if there is a loss of catalytic activity, it is very slow and undetectable over the 20 h on stream. It should be noted that some loss of activity could be compensated for by the reaction exotherm, more significant at high conversions. However, under constant reaction flow conditions at steady state, the gradual decrease in conversion should still be noticeable were catalyst deactivation appreciable. Deactivation of supported Pt catalysts in CO oxidation has been studied in great detail, see reference [26] and references therein. The conditions used in this study, a 30-fold excess of oxygen relative to reaction stoichiometry, would ensure the dominance of

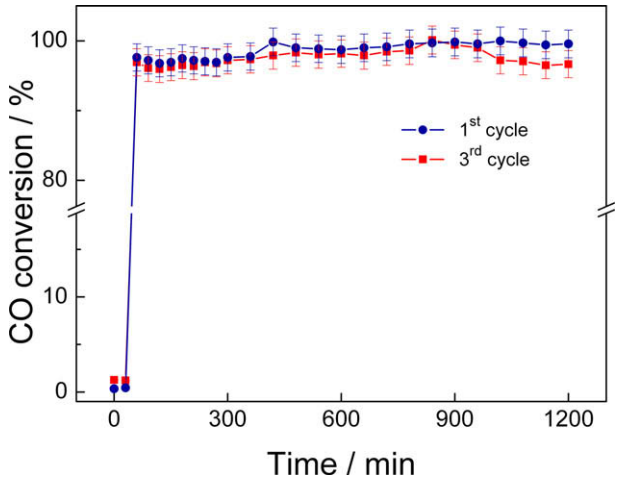

Fig. 9. Steady-state CO conversion extended and repeated runs with the 0.9 wt% Pt/PSi catalyst. First and third 20-h cycles are shown. Gas flow rate: 75 cm^3 min^{-1} at T = 150 °C, P = 1 bar. Error bars represent 3% experimental accuracy.

oxygen-sorbed species and would limit the effect of rearrangement of sorption sites and the increase in CO coverage, which has been identified as a dominant deactivation mechanism in the case of a near stoichiometric gas composition [26].

4. Conclusions

Pt nanoparticles were synthesised by *in situ* reduction of precursor salts by the hydrogen-terminated extended surface of porous nanocrystalline silicon. Careful control of the reaction conditions enable synthesis of noble metal nanoparticles inside the porous structure of silicon and having a well-controlled size distribution.

There are two key features that differentiate PSi matrix from other better-known support materials for noble metal nanoparticles, which result from high chemical reactivity of the extended H-terminated surface and the undulated, interconnected pore morphology. Highly reactive internal surface allows to synthesise metal nanoparticles *via* an *in situ* reaction without the use of additional reducing agents. However, as it was shown in this study, the synthesised metal nanoparticles are not completely reduced. The morphology of porous silicon enables easy mass transport of reactants and products through an open interconnected porous network, while retaining a reasonably high surface area, due to the mesopore range of pore diameters. High thermal stability of the prepared metal nanoparticles was observed. This can potentially be attributed to the effect of the pore morphology, however, this may also result from the formation of silicon oxide over-layer, protecting individual metal nanoparticles from sintering. The Pt/PSi catalysts were shown to be stable in continuous reaction cycles over cumulative 60 h on stream.

Acknowledgments

This work was in part funded by Engineering and Physical Sciences Research Council via Grant EP/E012183/1. We are grateful to Professor Adam F. Lee of Cardiff University for performing the H_2 dispersion measurements.

References

[1] M.V. Twigg (Ed.), Catalyst Handbook, second ed., Manson Publishing Ltd., 1996.
[2] G.P. Chiusoli, P.M. Maitlis (Eds.), Metal-catalysis in Industrial Organic Processes, Royal Society of Chemistry, Cambridge, 2006.
[3] T. Ioannides, X.E. Verykios, J. Catal. 161 (1996) 560–569.
[4] B. Coq, F. Figueras, Coordin. Chem. Rev. 178–180 (1998) 1753–1783.
[5] X.H. Chen, M. Moskovits, Nanoletters 7 (2007) 807–812.
[6] S. Polisski et al., Phys. Status Solidi (RRL) 2 (2008) 132–134.
[7] D.L. Fisher et al., Mater. Res. Soc. Symp. Proc. 358 (1995) 507–518.
[8] N. Künzner et al., J. Appl. Phys. 94 (2003) 4913–4917.
[9] D. Xu et al., New J. Chem. 27 (2002) 300–306.
[10] D. Clement et al., Phys. Status Solidi A 202 (2005) 1357.
[11] L.A. DeLouise, B.L. Miller, Anal. Chem. 77 (2005) 1950–1956.
[12] M. Bengtsson et al., Talanta 56 (2002) 341–353.
[13] I. Coulthard et al., Langmuir 9 (1993) 3441–3445.
[14] I. Coulthard et al., Phys. Status Solidi A 182 (2000) 157–162.
[15] I. Coulthard, T.K. Sham, Solid State Commun. 105 (1998) 751–754.
[16] C. Baratto et al., Sensors Actuat. B 68 (2000) 74–80.
[17] E.S. Lokteva et al., Kinet. Catal. 49 (2008) 748–755.
[18] S. Limaye et al., Phys. Status Solidi A 204 (2007) 1297–1301.
[19] R.W. Fathauer et al., Appl. Phys. Lett. 60 (1992) 995–997.
[20] J.N. Kidder et al., Appl. Phys. Lett. 61 (1992) 2896–2898.
[21] L.T. Canham, Appl. Phys. Lett. 57 (1990) 1046–1048.
[22] S. Doniach, M. Sunjic, J. Phys. C: Solid State Phys. 3 (1970) 285–291.
[23] E.P. Barrett, L.G. Joyner, P.P. Halenda, J. Am. Chem. Soc. 73 (1951) 373–380.
[24] J. Sarkany, D. Gonzales, Appl. Catal. 4 (1982) 53–66.
[25] J. Sarkany, R.D. Gonzales, Appl. Catal. 5 (1983) 85–97.
[26] N.W. Cant, D.E. Angove, J. Catal. 97 (1986) 36–42.
[27] A. Lapkin et al., Catal. Today 81 (2003) 611–622.
[28] A.G. Cullies, L.T. Canham, P.D.J. Calcott, Appl. Phys. Rev. 82 (1997) 909–965.
[29] A.J. Uhlir, Bell Syst. Technol. J. 35 (1956) 333–347.
[30] Y.H. Ogata et al., J. Porous Mater. 7 (2000) 63–66.
[31] J.E. Bateman et al., Chem. Commun. 23 (1997) 2275–2276.
[32] J. Yin et al., Surf. Coat. Technol. 198 (2005) 329–334.
[33] N.H. Zoubir, M. Vergnat, Appl. Surf. Sci. 89 (1995) 35–38.
[34] S.M. McClure, D.W. Goodman, Chem. Phys. Lett. 469 (2009) 1–13.
[35] A. Wootsch et al., Appl. Surf. Sci. 253 (2006) 1310–1322.
[36] S. Kapoor et al., Mater. Res. Bull. 40 (2005) 1654–1661.
[37] A. Bourane, D. Bianchi, J. Catal. 209 (2002) 114–125.